Chemistry–A European Journal
Research Article
doi.org/10.1002/chem.202202984
Chemistry Europe
European Chemical Societies Publishing
www.chemeurj.org

Structure Determination of the Crystalline LiPON Model Structure $Li_{5+x}P_2O_{6-x}N_{1+x}$ with $x \approx 0.9$

Stefanie Schneider,[a] Lucas G. Balzat,[a, b] Bettina V. Lotsch,[a, b] and Wolfgang Schnick*[a]

Abstract: Non-crystalline lithium oxonitridophosphate (LiPON) is used as solid electrolyte in all-solid-state batteries. Crystalline lithium oxonitridophosphates are important model structures to retrieve analytical information that can be used to understand amorphous phases better. The new crystalline lithium oxonitridophosphate $Li_{5+x}P_2O_{6-x}N_{1+x}$ was synthesized as an off-white powder by ampoule synthesis at 750–800 °C under Ar atmosphere. It crystallizes in the monoclinic space group $P2_1/c$ with $a = 15.13087(11)$ Å, $b = 9.70682(9)$ Å, $c = 8.88681(7)$ Å, and $\beta = 106.8653(8)°$. Two $P(O,N)_4$ tetrahedra connected by an N atom form the structural motif $[P_2O_{6-x}N_{1+x}]^{(5+x)-}$. The structure was elucidated from X-ray diffraction data and the model corroborated by NMR and infrared spectroscopy, and elemental analyses. Measurements of ionic conductivity show a total ionic conductivity of 6.8×10^{-7} S cm^{-1} at 75 °C with an activation energy of 0.52 ± 0.01 eV.

Introduction

Lithium oxonitridophosphates (LiPON) have gained attention over the past 30 years due to their Li^+ ion conductivity.[1–4] They develop stable solid electrolyte interfaces (SEI) in contact with Li[5,6] and therefore have found application as solid electrolytes (SE) within thin film all-solid-state batteries (SSBs).[7,8] Conceptually, SSBs provide the possibility of miniaturization of energy carriers with higher energy densities and better safety features than can be achieved with batteries based on liquid electrolytes.[6,9–12] In particular, the electrolytes used in SSBs are not flammable in contrast to the organic liquids conventionally used,[13,14] making them an excellent choice for application in medical devices like pacemakers.[15]

For miniaturization, solid electrolytes have to be applied in thin films, which is mostly achieved by sputtering lithium phosphate species in N_2-atmosphere onto a substrate.[1,2,4,16,17] The amorphous thin films obtained in this way have the advantage of mitigating grain boundary effects and enabling a high conductivity due to short diffusion pathways.[18]

However, structural analysis of amorphous materials – thin films or bulk – is always challenging. Absence of long-range order prevents classical diffraction methods like single-crystal X-ray diffraction or neutron powder diffraction. Instead, solid-state nuclear magnetic resonance (ssNMR) is a highly powerful tool to analyze local structure and especially the phosphate species present.[19,20] The anion sublattice plays a major role in Li^+ ion conductivity, as the Coulomb attraction towards Li^+ can be varied by the connectivity of the anionic species. Whereas non-condensed PO_4-tetrahedra exhibit strong Coulomb attraction towards Li^+, the net charge of one-dimensionally condensed chains (PO_3) is reduced, lowering attraction towards Li^+. Substitution of N for O in phosphate networks promotes condensation of $P(O,N)_4$-tetrahedra, leading to increased conductivity. Nitrogen atoms are versatile and can take doubly or triply bridging or even terminal positions. Whereas bridging N increase conductivity by the aforementioned mechanism, terminal N can hamper conductivity due to the higher charge Li^+ ions are exposed to.[21]

Whereas the search for amorphous LiPON materials with high ionic conductivities is important for their practical application as solid electrolyte materials, crystalline LiPON can help understand the intricacies of this system.[21–23] This can facilitate the development of the former. To date, only four crystalline phases in the quaternary system Li–P–O–N have been characterized crystallographically, namely $Li_{2.88}PO_{3.73}N_{0.14}$, Li_2PO_2N, $Li_{14}(PON_3)_2O$, and $Li_{3.6}PO_{3.4}N_{0.6}$.[20,24–26]

$Li_{2.88}PO_{3.73}N_{0.14}$ crystallizes isotypically to the three-dimensionally connected γ-Li_3PO_4 with both $P(O,N)_4$ and $Li(O,N)_4$ tetrahedra and is synthesized by heating Li_3N with $LiPO_3$ in N_2 gas flow. $P(O,N)_4$ tetrahedra are completely surrounded by $Li(O,N)_4$ tetrahedra.[24] Li_2PO_2N is prepared from Li_2O, P_2O_5, and P_3N_5 at 950 °C. Its structure comprises corner-sharing tetrahedra forming chains that are separated by Li^+ ions.[25] $Li_{3.6}PO_{3.4}N_{0.6}$ is obtained from $LiPO_3$ and Li_3N through mechanical milling for 20 min under Ar. Its structure consists of non-condensed, statistically disordered $[PO_2N_2]^{5-}$, $[PO_3N]^{4-}$, and $[PO_4]^{3-}$ tetrahedra.[20]

[a] S. Schneider, L. G. Balzat, Prof. Dr. B. V. Lotsch, Prof. Dr. W. Schnick
Department of Chemistry
University of Munich (LMU)
Butenandtstraße 5–13, (D) 81377 Munich (Germany)
E-mail: wolfgang.schnick@uni-muenchen.de
[b] L. G. Balzat, Prof. Dr. B. V. Lotsch
MPI for Solid State Research
Department of Nanochemistry
Heisenbergstraße 1, (D) 70569 Stuttgart (Germany)

Supporting information for this article is available on the WWW under https://doi.org/10.1002/chem.202202984

$Li_{14}(PON_3)_2O$, synthesized from $PO(NH_2)_3$ and $LiNH_2$, was the first oxonitridophosphate comprising non-condensed PON_3 tetrahedra. It also contains O^{2-} ions, making it a lithium oxonitridophosphate oxide.[26] Impedance measurements have not been carried out for this material as yet.

As can be seen in Figure 1, the existing structural motifs are limited to isolated tetrahedra and one-dimensional chains of corner-sharing tetrahedra. Thus, ab-initio calculations for the diffusion of Li^+ in a hypothetical crystalline LiPON material are often carried out using lithium phosphates as starting point. Besides non-condensed Li_3PO_4 phases, $Li_4P_2O_7$, which contains diphosphate anions, has been considered, in which bridging O were substituted by N. This results in the sum formula $Li_5P_2O_6N$, which was assumed to crystallize in $P\bar{1}$, as $Li_4P_2O_7$ does.[19,27]

In this work, we present the synthesis and thorough characterization of a new crystalline lithium oxonitridophosphate, namely $Li_{5+x}P_2O_{6-x}N_{1+x}$. This compound contains $[P_2O_{6-x}N_{1+x}]^{(5+x)-}$ oxonitridodiphosphate anions, a motif that has not been reported in lithium oxonitridophosphates so far. With the spectroscopic and diffraction information collected from this compound, structural models for ab initio calculations on conductivity and NMR spectroscopic data of amorphous films can be improved.

Results and Discussion

Synthesis

$Li_{5+x}P_2O_{6-x}N_{1+x}$ was prepared from P_3N_5, Li_3N, and Li_2O in a 4:7:20 molar ratio under Ar atmosphere in an open Ta crucible that was placed in a sealed silica ampoule. The mixture was heated at 300 K h^{-1}, held at 760 °C for 90 h and cooled with a rate of 300 K h^{-1}. The reaction is very sensitive to changes in reaction conditions and side phases like $Li_{10}P_4N_{10}$ can occur.[28]

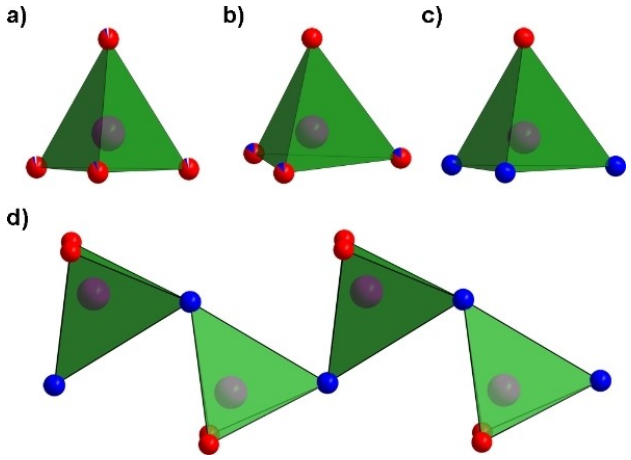

Figure 1. Structural motifs in known crystalline lithium oxonitridophosphates. P atoms are displayed in pink, O and N are displayed in red and blue, respectively. a-c) isolated tetrahedra with mixed and full occupations of O/N positions.[20,24,26] d) chain of tetrahedra.[25]

As in lithium nitridophosphate syntheses, Li_3P is a common byproduct, especially at long reaction times and higher temperatures.[28–32] Large amounts of Li_2O remained in all samples. Stoichiometric amounts of starting materials as stated in the idealized balanced reaction Equation (1) did not yield the title compound in a phase pure state.

$$2\ P_3N_5 + (18 - 3x)\ Li_2O \rightarrow 3\ Li_{5+x}P_2O_{6-x}N_{1+x} + (7 - 3x)\ Li_3N \quad (1)$$

Instead, Li_3N had to be introduced as starting material. This is in accordance with lithium nitridophosphate synthesis, in which an excess of Li_3N had to be used to achieve a Li_3N self-flux.[28–31] Furthermore, additional incorporation of N into the structure necessitates larger amounts of Li_3N as nitrogen source. Figure 2 shows the Rietveld refinement for a sample with Li_2O (15%) and small amounts of $Li_{10}P_4N_{10}$ (< 1 %) and Li_3P (< 1 %) as byproducts. Li_3P can largely be removed by washing the sample with dry ethanol. Soaking in dry ethanol additionally reduces Li_2O content, but also slowly decomposes $Li_{5+x}P_2O_{6-x}N_{1+x}$.

Crystal structure

The crystal structure was solved using both single-crystal and powder X-ray diffraction data. Due to small crystal sizes, only data sets of poor quality were collected with single-crystal X-ray diffraction. However, cell parameters and the space group were determined and subsequently used to solve the structure from X-ray powder diffraction data. For additional crystallographic data, see Table 1 and Tables S1–S3 (Supporting Information).

$Li_{5+x}P_2O_{6-x}N_{1+x}$ crystallizes in the monoclinic space group $P2_1/c$ (no. 14) with lattice parameters $a = 15.13087(11)$ Å, $b = 9.70682(9)$ Å, $c = 8.88681(7)$ Å, and $\beta = 106.8653(8)°$. The structure comprises pairs of corner-sharing $P(O,N)_4$ tetrahedra connected by

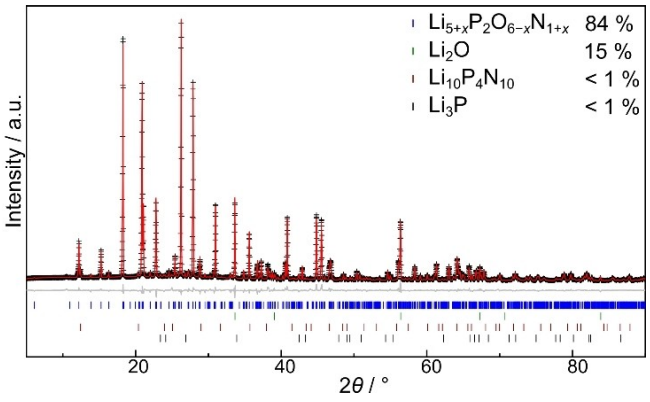

Figure 2. Rietveld refinement for $Li_{5+x}P_2O_{6-x}N_{1+x}$ with observed (black crosses) and calculated (red line) intensities, and difference (gray line). Positions of possible Bragg reflections of $Li_{5+x}P_2O_{6-x}N_{1+x}$, Li_2O, $Li_{10}P_4N_{10}$, and Li_3P are shown with blue, green, brown, and black tick marks, respectively. Fractions of the respective phases are given in wt-%.

Table 1. Crystallographic details on $Li_{5+x}P_2O_{6-x}N_{1+x}$. Standard deviations are given in parentheses.

formula	$Li_{5+x}P_2O_{6-x}N_{1+x}$
formula mass [g mol^{-1}]	206.66
crystal system/ space group type	monoclinic $P2_1/c$ (no. 14)
lattice parameters [Å, °]	$a = 15.13087(11)$
	$b = 9.70682(9)$
	$c = 8.88681(7)$
	$\beta = 106.8653(8)$
cell volume [Å^3]	1249.091(18)
formula units per cell Z	8
X-ray density [g cm^3]	2.198(1)
Absorption coefficient [cm^{-1}]	62.63
radiation	$Cu_{K\alpha1}$ ($\lambda = 1.540596$ Å)
monochromator	Ge(1 1 1)
diffractometer	Stoe StadiP
detector	Mythen 1 K linear PSD
2θ range [°]	5–101
temperature [K]	297(2)
data points	6432
number of observed reflections	1337
number of parameters	119
program used	TOPAS 6
structure refinement	Rietveld method
profile function	fundamental parameters
background function	shifted Chebychev
terms (backgr. function)	12
R_{wp}	0.064
R_{exp}	0.023
R_p	0.046
R_{Bragg}	0.032
X^2	2.793

N. Two crystallographically different $[P_2O_{6-x}N_{1+x}]^{(5+x)-}$ diphosphate anions occur with altogether four crystallographically different P positions. The bridging atoms are assumed to be N, as substitution of bridging atoms by N is energetically favorable in contrast to bridging O-atoms (Figure 3).[21,27,33] Due to the very similar atomic form factors of O and N, the atom types cannot be determined unequivocally by X-ray diffraction. Mixed occupancy of additional O positions would lead to a higher negative charge of the structural motif and could be balanced by partial or full occupation of additional Li^+ positions. This issue can be considered with the sum formula $Li_{5+x}P_2O_{6-x}N_{1+x}$.

P–N bond lengths vary between 1.60(2)–1.75(2) Å, P–O bond lengths between 1.510(13) and 1.681(14) Å. These values are within the normal range for known P–N/O distances in reported crystalline LiPON phases.[20,24–26]

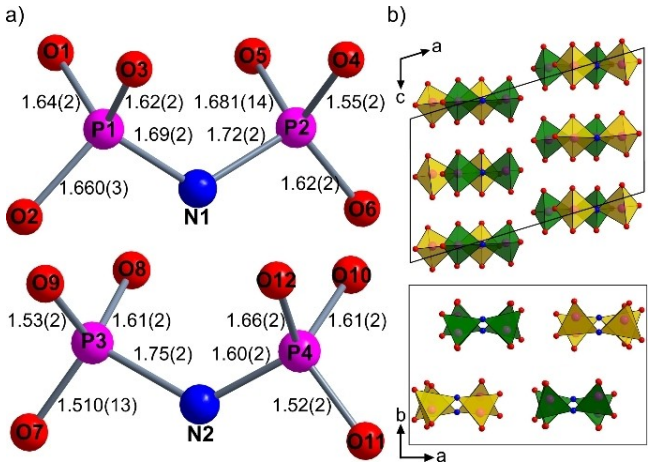

Figure 3. Structural motifs in $Li_{5+x}P_2O_{6-x}N_{1+x}$. a) Vertex-sharing pairs of PO_3N-tetrahedra with bond lengths in Å. O-positions can also have mixed occupation with N. b) Unit cells with the two crystallographically different $[P_2O_{6-x}N_{1+x}]^{(5+x)-}$ motifs in yellow and green.

Nuclear magnetic resonance spectroscopy

^{31}P, ^6Li and ^7Li NMR measurements were performed. If no mixed occupation O/N is assumed, four distinct P positions can be expected to result in four signals with shifts around 14.2 ppm. Two distinct signals at 21.4 and 14.2 ppm are visible (Figure 4). For two PO_3N tetrahedra bridged by N, measurements in amorphous LiPON showed an isotropic shift $\delta_{iso}(^{31}P) = 14.6$ ppm, while ab initio molecular dynamics (AIMD) simulations predict a shift of $\delta_{iso} = 12.77$ ppm.[19] This corresponds well with the observed $\delta = 14.2$ ppm. Furthermore, the deconvolution of NMR signals of amorphous LiPON shows a difference in shifts of about 10 ppm upon substituting the bridging O by N. In non-condensed phases, a shift difference of about 10 ppm is seen for each O substituted by N in the respective tetrahedron.[19] Thus, the second signal at 21.4 ppm is expected to be the result of additional incorporation of one N at an O atomic position, PO_2N_2. The breadth of the signals is probably a result of statistically distributed incorporation of N into the anionic motifs and of the two crystallographically different dimers being present. As there are only two signals at 14.2 and 21.4 ppm, the environment of P is assumed to hold a maximum of two N atoms. This would result in $Li_{5+x}P_2O_{6-x}N_{1+x}$ with $0 \leq x \leq 2$. Deconvolution of the two signals yielded a 53(2):47(2) ratio of the signals at 14.2 and 21.4 ppm, which corresponds to the presence of 94(4)% $[P_2O_5N_2]^{6-}$ and 6(4)% $[P_2O_6N]^{5-}$. This means that in 94(4)% of the dimers one additional N is inserted, leading to $0.90 \leq x \leq 0.98$. However, as this error margin is possibly an underestimation of the actual error, the more rough value of $x \approx 0.9$ will be used. More precise values could be obtained by additional O/N-sensitive analytical methods like neutron diffraction.

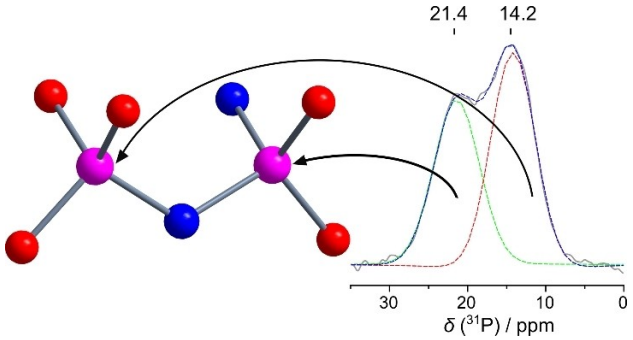

Figure 4. ^{31}P NMR spectrum of $Li_{5+x}P_2O_{6-x}N_{1+x}$ with corresponding tetrahedra. Signals were fitted with pseudo-Voigt functions.[38] P, O, and N are shown in pink, red, and blue, respectively.

^{6}Li and ^{7}Li NMR spectra show one broad signal at 1.15 and 2.9 ppm, respectively, indicating only very low mobility of Li^{+} (Figures S2 and S3).[34,35] To extract information on Li dynamics, variable temperature measurements would be necessary.[34,36,37]

FTIR and thermal stability measurements

Infrared (IR) spectroscopic measurements were conducted in order to rule out the presence of hydrogen in the structure. O–H or N–H vibrational bands should be visible in the area of 2800–3200 and 3000–3500 cm^{-1}, if hydrogen is present in the structure. However, no peaks are visible in this area (Figure 5).[39–41] The fingerprint area between 400–1200 cm^{-1} contains six distinct signals. Possibly, some modes are superimposed and cannot be resolved. Modes in the area of 900–1100 cm^{-1} correspond to stretching vibrations of P–N, P–O and P–N–P, whereas those in the area of 500–550 cm^{-1} result from bending modes of P–N–P and O–P–O.[39–42] The sharp signal at 785 cm^{-1} might be caused by asymmetric stretching modes of P–N–P, as was proposed for short chains within lithium oxonitridophosphates.[43] Furthermore, the width of the signals at ca. 500 cm^{-1} might also result from underlying Li–O/N vibrations.[43,44]

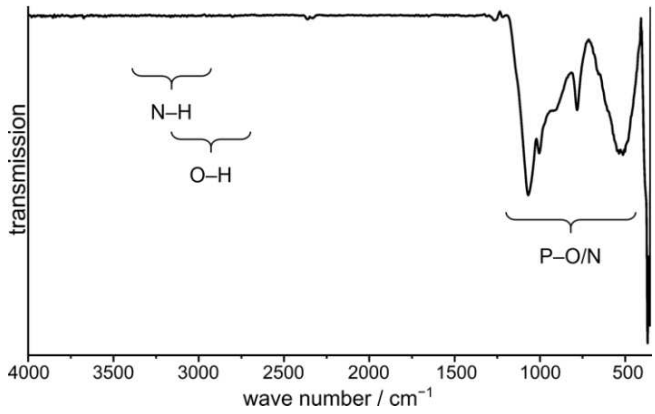

Figure 5. Infrared spectrum of $Li_{5+x}P_2O_{6-x}N_{1+x}$ measured with an ATR unit. No O–H or N–H peaks are visible. Small signals at 2366 cm^{-1} can be explained by partial hydrolysis of the sample surface.

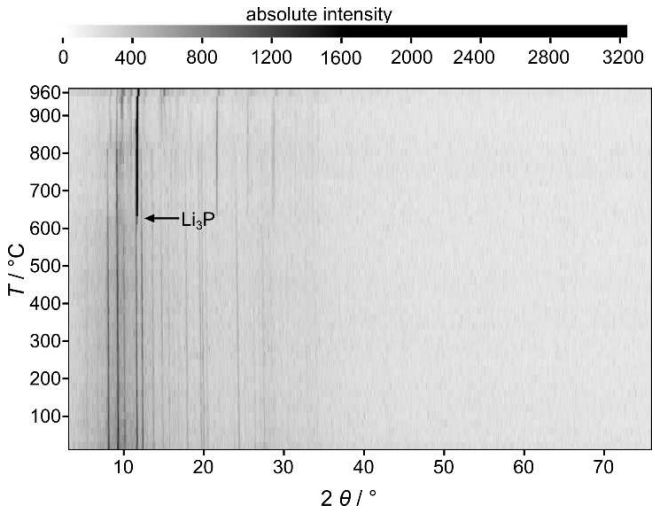

Figure 6. Temperature-dependent X-ray powder diffraction ($Mo_{K\alpha1}$ $\lambda = 0.70930$ Å) data shows $Li_{5+x}P_2O_{6-x}N_{1+x}$ up to 900 °C, with decomposition towards Li_3P beginning at 640 °C.

$Li_{5+x}P_2O_{6-x}N_{1+x}$ is thermally stable up to 620 °C. At 640 °C, incipient decomposition of $Li_{5+x}P_2O_{6-x}N_{1+x}$ to Li_3P is visible in temperature-dependent PXRD (Figure 6). Reflections of $Li_{5+x}P_2O_{6-x}N_{1+x}$ are visible up to 800 °C, above which only Li_3P is visible. This is in good agreement with other lithium nitridophosphates[28–31] and with the observation of Li_3P as side phase at syntheses with higher reaction temperature. Upon cooling, only Li_3P remains in the sample.

Elemental analysis is hindered by the compound's composition, side phases and sensitivity to hydrolysis. Electron-dispersive X-ray spectroscopy (EDX), inductively-coupled plasma optical emission spectroscopy (ICP-OES), and combustion analysis (CHNS) was performed. However, light elements are not (Li) or not reliably (O,N) detected by EDX. ICP-OES can only detect Li and P, which is confounded by Li-containing side phases (mainly Li_2O, and residues of $Li_{10}P_4N_{10}$). CHNS can only give absolute values for N, but due to hydrolysis during the weighing process, these results are also falsified. Thus, elemental analysis (EDX) was only deployed to confirm that no other elements are present in the sample.

Determination of the ionic conductivity

The ionic conductivity of $Li_{5+x}P_2O_{6-x}N_{1+x}$ was determined through electrochemical impedance spectroscopy (EIS). All measured samples contained Li_2O and $Li_{10}P_4N_{10}$ as side phases. EIS data of $Li_{5+x}P_2O_{6-x}N_{1+x}$ measured at 75 °C are shown in a Nyquist plot in Figure 7. All temperature-dependent EIS spectra are shown in Figure S4. The data were fitted with an equivalent circuit containing two circuits in series, containing each a resistor and a constant phase element (CPE) in parallel. Polarization was modeled with an additional CPE in series. CPEs were chosen to account for non-ideal sample behavior.[45] The capacities of CPE1 and CPE2 were calculated using the Brug formula.[46] The capacities at 75 °C of CPE1 and CPE2 are 2.9×10^{-11} F and 1.1×10^{-10} F, respectively. Therefore, the first process modeled by R1/CPE1 was assigned to the bulk ionic conductivity of $Li_{5+x}P_2O_{6-x}N_{1+x}$.[47] The bulk ionic conductivity was calculated using the resistance R1 and is 2.2×10^{-7} S cm^{-1} at 25 °C and 1.4×10^{-6} S cm^{-1} at 75 °C. The second semi-circle modeled by R2/CPE2 could stem from grain boundaries or ionic contributions from the impurity side phase $Li_{10}P_4N_{10}$, but an unambiguous assignment was not possible.[28,47] The total ionic conductivity of $Li_{5+x}P_2O_{6-x}N_{1+x}$ was calculated from the total resistance (R1 + R2) and amounts to 4.6×10^{-8} S cm^{-1} at 25 °C and 6.8×10^{-7} S cm^{-1} at 75 °C.

The total activation energy of $Li_{5+x}P_2O_{6-x}N_{1+x}$ was obtained by fitting temperature-dependent EIS data to a linear Arrhenius-type behavior. The corresponding Arrhenius plot is shown in the inset in Figure 7. The total activation energy for

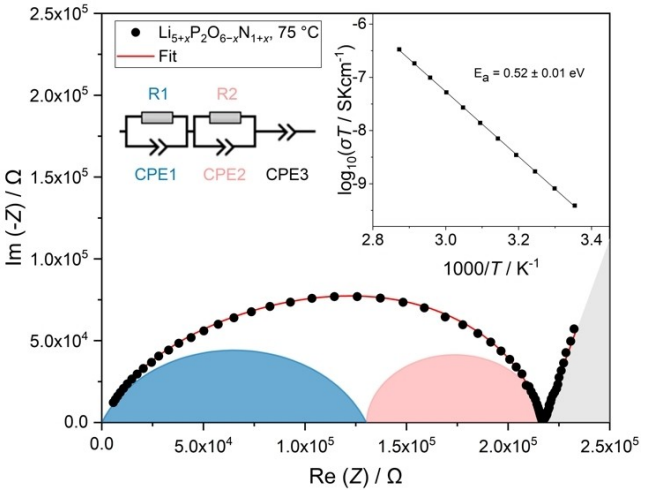

Figure 7. Nyquist plot of $Li_{5+x}P_2O_{6-x}N_{1+x}$ at 75 °C. The data were modelled using an R1/CPE1-R2/CPE2-CPE3 model. The contributions of the different circuit elements have been highlighted. The inset shows an Arrhenius plot obtained from temperature-dependent EIS measurements resulting in an activation energy of 0.52 ± 0.01 eV for $Li_{5+x}P_2O_{6-x}N_{1+x}$.

$Li_{5+x}P_2O_{6-x}N_{1+x}$ is 0.52 ± 0.01 eV. Both the ionic conductivity and activation energy lie well in the expected range for LiPON materials (e.g.: LiPON, 1.6×10^{-6} S cm^{-1}, 0.58 eV; $Li_{3.6}PO_{3.4}N_{0.6}$, 5.6×10^{-8} S cm^{-1}, 0.55 eV; all values at 25 °C).[20,22,24,25,48]

Since no completely phase-pure samples of $Li_{5+x}P_2O_{6-x}N_{1+x}$ were obtained, several samples were measured to confirm the obtained ionic conductivity and activation energy. All samples gave similar values for ionic conductivity and activation energy. The EIS data for two different samples of $Li_{5+x}P_2O_{6-x}N_{1+x}$ are shown in the Supporting Information as representative examples (Figures S4–S6, Tables S7–S9).

Conclusion

The lithium oxonitridophosphate $Li_{5+x}P_2O_{6-x}N_{1+x}$ was prepared from ampoule synthesis. It crystallizes in space group $P2_1/c$ with $a = 15.13087(11)$ Å, $b = 9.70682(9)$ Å, $c = 8.88681(7)$ Å, and $\beta = 106.8653(8)°$. The structure consists of corner-sharing tetrahedra, similar to $Li_4P_2O_7$.[49–53] N does not only occupy bridging positions, but also terminal ones. Stoichiometric use of starting materials does not produce $Li_{5+x}P_2O_{6-x}N_{1+x}$ ($x = 0$). Instead, Li_3N had to be used to obtain the phase, but also results in x≈ 0.93 due to the additional N source material.

The total ionic conductivity of 4.6×10^{-8} S cm^{-1} at 25 °C puts $Li_{5+x}P_2O_{6-x}N_{1+x}$ into a range comparable to that of amorphous LiPON.[3,48] Grain boundary effects restrict Li^+ movement, reducing applicability in all-solid-state batteries.[18,54]

Nonetheless, with the structural and spectroscopic information obtained from $Li_{5+x}P_2O_{6-x}N_{1+x}$, structural models for amorphous LiPON films can be improved in their accuracy. Furthermore, analytics of LiPON thin films – especially NMR – can benefit from this, as local structure observed by NMR in amorphous materials can be cross-checked with crystalline references. Finally, this compound might be employed as a model structure for the computational investigation of conduction pathways. In the future, neutron diffraction experiments should be conducted for more detailed information on O/N occupation.

Experimental Section

Synthesis of P_3N_5:[55] P_4S_{10} (Acros Organics, >99.8%) was transferred to a dry quartz tube in argon counterflow. The starting material was saturated with a stream of ammonia (Air liquide, 99.999%) (4 h) at room temperature, heated with a rate of 5 K min^{-1} in a constant flow of ammonia and held at 850 °C for 4 h. After cooling down (5 K min^{-1}), the orange product was removed from the tube, washed with water, ethanol, and acetone, and dried. The obtained product was analyzed using powder X-ray diffraction. Presence of hydrogen in the sample was ruled out using infrared spectroscopy and elemental analysis CHNS. The obtained P_3N_5 was used for synthesis of the title compound.

Synthesis of $Li_{5+x}P_2O_{6-x}N_{1+x}$: P_3N_5, Li_3N (Rockwood, 99.999%), and Li_2O (Alfa Aesar, 99.5%) were combined and ground in an agate mortar in inert atmosphere using an argon-filled glovebox (Unilab, MBraun, Garching, O_2 <1 ppm, H_2O <1 ppm). The mixture was transferred to a Ta crucible within a silica tube with a long funnel in argon counterflow. Silica ampoules were sealed off using a vacuum line with argon and an oxyhydrogen burner (all gasses: Air Liquide, 99.999%). Ampoules were heated at 5 K min^{-1} to 800 °C and held for 90 h. The samples were cooled to room temperature at a rate of 5 K min^{-1}.

Powder X-ray diffraction: Samples were sealed into glass capillaries (diameter 0.5 mm, wall thickness 0.01 mm, Hilgenberg GmbH). Data was collected using a Stoe STADI P diffractometer with $Cu_{K\alpha1}$ radiation ($\lambda = 1.5406$ Å), Ge(1 1 1) monochromator and Mythen 1 K detector in Debye-Scherrer geometry. Structure solution and Rietveld refinement was performed using the TOPAS-Academic software package.[56] After extraction of intensities using a Pawley fit, the structure was solved using a charge flipping algorithm.[57–59] A shifted-Chebyshev function was used for the background and peak shapes were refined using the fundamental parameters approach.[60,61]

Single-crystal X-ray diffraction: Single crystals were selected under dried paraffin oil and sealed into oil-filled glass capillaries (diameter 0.1 mm, wall thickness 0.01 mm, Hilgenberg GmbH). Data was acquired using a D8 Venture diffractometer (Bruker, Billerica MA, USA), with $Mo_{K\alpha}$ radiation ($\lambda = 0.71073$ Å) from a rotating anode. Cell parameters were determined and precession images were generated using the APEX3 program package.[62]

Deposition Number(s) 2191662 contain(s) the supplementary crystallographic data for this paper. These data are provided free of charge by the joint Cambridge Crystallographic Data Centre and Fachinformationszentrum Karlsruhe Access Structures service.

Temperature-dependent X-ray diffraction: A Stoe STADI P diffractometer using $Mo_{K\alpha}$ radiation ($\lambda = 0.71073$ Å) and a Ge(1 1 1) monochromator in Debye-Scherrer geometry, equipped with a graphite furnace and an imaging plate position sensitive detector was used to take temperature-dependent powder X-ray data. The sample was sealed into a glass capillary (diameter 0.3 mm, wall thickness 0.01 mm, Hilgenberg GmbH) and closed with a clog of vacuum grease (Leybonol, LVO 810 Lithelen). Measurements were taken every 20 K starting at room temperature up to 1000 °C, with a heating rate of 5 K min^{-1}.

Solid-state magic angle spinning (MAS) NMR methods: NMR spectra were collected on ^{6}Li, ^{7}Li, and ^{31}P with a DSX AVANCE spectrometer (Bruker) with a magnetic field of 11.7 T. The $Li_{5+x}P_2O_{6-x}N_{1+x}$ sample was filled into a rotor with a diameter of 2.5 mm, which was mounted on a commercial MAS probe (Bruker) and spun with a rotation frequency of 25 kHz. The obtained data was analyzed using device-specific software.[63]

Fourier-transform infrared (FTIR) spectroscopy: FTIR measurements were performed on a woodpecker cell with a window of CsBr using a Vertex-80V-FTIR spectrometer by Bruker. Data was collected at room temperature under static vacuum (ca. 5 mbar) in the range of 400–4000 cm^{-1}. Data was acquired using OPUS 6.5[64] and illustrated using Origin.[38]

Elemental analysis: Energy-dispersive X-ray spectroscopy (EDX): EDX measurements were performed at a Dualbeam Helios Nanolab G3 UC (FEI) scanning electron microscope featuring an EDX detector (X-Max 80 SDD, Oxford instruments). The samples were positioned on adhesive carbon pads. A conductive carbon film was applied using a high-vacuum sputter coater (BAL-TEC MED 020, Bal Tec A). Multiple particles were targeted using an accelerating voltage of 20 kV.

Inductively coupled plasma optical emission spectrometry (ICP OES): Elemental analysis was conducted at a Varian Vista RL with a 40 MHz RF generator, and a VistaChip CCD detector.

Mass spectrometry: CHNS spectrometry was performed using a Vario MICRO Cube device (Elementar, Langenselbold, Germany).

Ionic conductivity measurements: Electrochemical impedance spectroscopy (EIS) was performed using an Ivium compactstat.h potentiostat (24 bit instrument) in a two-electrode setup with a RHD Instruments Microcell HC cell stand loaded with a RHD Instruments TSC battery cell. Before EIS measurements were carried out, all samples were thoroughly ground in an agate mortar and subsequently compacted into pills with a thickness of about 0.3 mm and a diameter of 5 mm using uniaxial cold-pressing (p $\approx$ 2 t). To ensure good contact during EIS, all pills were sputtered with ruthenium metal using a Quorum Q150 GB sputter coater. All samples were measured in the frequency range of 1 MHz-0.1 Hz and an excitation voltage of 100 mV. Temperature-dependent data was gathered from 25–75 °C in 5 °C steps and an equilibration time of 1 h. All samples were prepared and measured in an argon-filled glovebox (MB200, MBraun, Garching, $O_2 < 0.1$ ppm, $H_2O < 1$ ppm). Data analysis and fitting procedures were carried out with the software RelaxIS3 (RHD instruments, Darmstadt).

Acknowledgements

The authors thank Lisa Gamperl, Christian Minke, Valentin Bockmaier, and Sandra Albrecht for EDX, NMR, FTIR, and ICP-OES measurements, respectively (all at Department of Chemistry, LMU Munich). The authors acknowledge funding support from the Deutsche Forschungsgemeinschaft (DFG, German Research Foundation) under Germany's Excellence Strategy-EXC 2089/1-390776260 (e-conversion). L.G.B. and B.V.L. acknowledge financial support by the German Federal Ministry of Research and Education (BMBF), project 03XP0177B (FestBatt). Open Access funding enabled and organized by Projekt DEAL.

Conflict of Interest

The authors declare no conflict of interest.

Data Availability Statement

The data that support the findings of this study are available in the supplementary material of this article.

Keywords: conducting materials · lithium · nitrides · NMR spectroscopy · solid-state structures

[1] J. B. Bates, N. J. Dudney, G. R. Gruzalski, R. A. Zuhr, A. Choudhury, C. F. Luck, J. D. Robertson, *Solid State Ionics* **1992**, *53–56*, 647–654.
[2] J. B. Bates, N. J. Dudney, G. R. Gruzalski, R. A. Zuhr, A. Choudhury, C. F. Luck, J. D. Robertson, *J. Power Sources* **1993**, *43*, 103–110.
[3] X. Yu, J. B. Bates, G. E. Jellison Jr., F. X. Hart, *J. Electrochem. Soc.* **1997**, *144*, 524.
[4] J. B. Bates, N. J. Dudney, B. Neudecker, A. Ueda, C. D. Evans, *Solid State Ionics* **2000**, *135*, 33–45.
[5] J. Janek, W. G. Zeier, *Nat. Energy* **2016**, *1*, 1–4.
[6] J. Schnell, T. Günther, T. Knoche, C. Vieider, L. Köhler, A. Just, M. Keller, S. Passerini, G. Reinhart, *J. Power Sources* **2018**, *382*, 160–175.
[7] F. Zheng, M. Kotobuki, S. Song, M. O. Lai, L. Lu, *J. Power Sources* **2018**, *389*, 198–213.
[8] J. D. LaCoste, A. Zakutayev, L. Fei, *J. Phys. Chem. C* **2021**, *125*, 3651–3667.
[9] J. G. Kim, B. Son, S. Mukherjee, N. Schuppert, A. Bates, O. Kwon, M. J. Choi, H. Y. Chung, S. Park, *J. Power Sources* **2015**, *282*, 299–322.
[10] W. Weppner, in *Encyclopedia of Electrochemical Power Sources*, Elsevier B.V., Amsterdam, **2009**, pp. 162–168.
[11] Y. Su, J. Falgenhauer, A. Polity, T. Leichtweiß, A. Kronenberger, J. Obel, S. Zhou, D. Schlettwein, J. Janek, B. K. Meyer, *Solid State Ionics* **2015**, *282*, 63–69.
[12] R. Chen, W. Qu, X. Guo, L. Li, F. Wu, *Mater. Horiz.* **2016**, *3*, 487–516.
[13] E. P. Roth, C. J. Orendorff, *Electrochem. Soc. Interface* **2012**, *21*, 45–49.
[14] Y. C. Jung, S. K. Kim, M. S. Kim, J. H. Lee, M. S. Han, D. H. Kim, W. C. Shin, M. Ue, D. W. Kim, *J. Power Sources* **2015**, *293*, 675–683.
[15] B. B. Owens, B. Scrosati, P. Reale, in *Encyclopedia of Electrochemical Power Sources*, Elsevier B.V., Amsterdam, **2009**, pp. 120–128.
[16] H. Y. Park, S. C. Nam, Y. C. Lim, K. G. Choi, K. C. Lee, G. B. Park, S. R. Lee, H. P. Kim, S. B. Cho, *J. Electroceram.* **2006**, *17*, 1023–1030.
[17] P. Birke, W. F. Chu, W. Weppner, *Solid State Ionics* **1996**, *93*, 1–15.
[18] J. A. Dawson, P. Canepa, T. Famprikis, C. Masquelier, M. S. Islam, *J. Am. Chem. Soc.* **2018**, *140*, 362–368.
[19] M. A. T. Marple, T. A. Wynn, D. Cheng, R. Shimizu, H. E. Mason, Y. S. Meng, *Angew. Chem. Int. Ed.* **2020**, *59*, 22185–22193; *Angew. Chem.* **2020**, *132*, 22369–22377.
[20] P. López-Aranguren, M. Reynaud, P. Głuchowski, A. Bustinza, M. Galceran, J. M. López Del Amo, M. Armand, M. Casas-Cabanas, *ACS Energy Lett.* **2021**, *6*, 445–450.
[21] V. Lacivita, N. Artrith, G. Ceder, *Chem. Mater.* **2018**, *30*, 7077–7090.
[22] A. Al-Qawasmeh, N. A. W. Holzwarth, *J. Power Sources* **2017**, *364*, 410–419.
[23] P. Henkel, D. Mollenhauer, *J. Comput. Chem.* **2021**, *42*, 1283–1295.
[24] B. Wang, B. C. Chakoumakos, B. C. Sales, B. S. Kwak, J. B. Bates, *J. Solid State Chem.* **1995**, *115*, 313–323.
[25] K. Senevirathne, C. S. Day, M. D. Gross, A. Lachgar, N. A. W. Holzwarth, *Solid State Ionics* **2013**, *233*, 95–101.
[26] D. Baumann, W. Schnick, *Eur. J. Inorg. Chem.* **2015**, *2015*, 617–621.
[27] Y. A. Du, N. A. W. Holzwarth, *Phys. Rev. B* **2010**, *81*, 1–15.
[28] E. M. Bertschler, C. Dietrich, T. Leichtweiß, J. Janek, W. Schnick, *Chem. Eur. J.* **2018**, *24*, 196–205.
[29] E. M. Bertschler, C. Dietrich, J. Janek, W. Schnick, *Chem. Eur. J.* **2017**, *23*, 2185–2191.
[30] E. M. Bertschler, R. Niklaus, W. Schnick, *Chem. Eur. J.* **2017**, *23*, 9592–9599.
[31] E. M. Bertschler, R. Niklaus, W. Schnick, *Chem. Eur. J.* **2018**, *24*, 736–742.

[32] E. M. Bertschler, T. Bräuniger, C. Dietrich, J. Janek, W. Schnick, *Angew. Chem. Int. Ed.* **2017**, *56*, 4806–4809; *Angew. Chem.* **2017**, *129*, 4884–4887.
[33] Y. A. Du, N. A. W. Holzwarth, *Phys. Rev. B* **2008**, *78*, 1–13.
[34] R. Böhmer, K. R. Jeffrey, M. Vogel, *Prog. Nucl. Magn. Reson. Spectrosc.* **2007**, *50*, 87–174.
[35] A. Kuhn, V. Duppel, B. V. Lotsch, *Energy Environ. Sci.* **2013**, *6*, 3548–3552.
[36] A. Kuhn, M. Kunze, P. Sreeraj, H. D. Wiemhöfer, V. Thangadurai, M. Wilkening, P. Heitjans, *Solid State Nucl. Magn. Reson.* **2012**, *42*, 2–8.
[37] A. Haffner, T. Bräuniger, D. Johrendt, *Angew. Chem. Int. Ed.* **2016**, *55*, 13585–13588; *Angew. Chem.* **2016**, *128*, 13783–13786.
[38] *Origin Pro 2018G*, Origin Lab Corporation, Northampton, USA, **2018**.
[39] W. Schnick, J. Lücke, *Z. Anorg. Allg. Chem.* **1992**, *610*, 121–126.
[40] S. Horstmann, E. Irran, W. Schnick, *Z. Anorg. Allg. Chem.* **1998**, *624*, 620–628.
[41] D. Baumann, W. Schnick, *Inorg. Chem.* **2014**, *53*, 7977–7982.
[42] K. Nakamoto, *Infrared and Raman Spectra of Inorganic and Coordination Compounds: Part A: Theory and Applications in Inorganic Chemistry: Sixth Edition*, John Wiley & Sons, Inc., Hoboken, NJ, **2008**.
[43] M. A. Carrillo Solano, M. Dussauze, P. Vinatier, L. Croguennec, E. I. Kamitsos, R. Hausbrand, W. Jaegermann, *Ionics* **2016**, *22*, 471–481.
[44] E. I. Kamitsos, G. D. Chryssikos, *Solid State Ionics* **1998**, *105*, 75–85.
[45] J. R. Macdonald, W. B. Johnson, in *Impedance Spectroscopy: Theory, Experiment, Applications, Second Ed.*, John Wiley & Sons, Inc., Hoboken, NJ, **2005**, pp. 1–26.
[46] G. J. Brug, A. L. G. van den Eeden, M. Sluyters-Rehbach, J. H. Sluyters, *J. Electroanal. Chem.* **1984**, *176*, 275–295.
[47] J. T. S. Irvine, D. C. Sinclair, A. R. West, *Adv. Mater.* **1990**, *2*, 132–138.
[48] S. Zhao, Z. Fu, Q. Qin, *Thin Solid Films* **2002**, *415*, 108–113.
[49] O. V. Yakubovich, O. K. Mel'nikov, *Kristallografiya* **1994**, *39*, 815–820.
[50] A. Daidouh, M. L. Veiga, C. Pico, M. Martinez-Ripoll, *Acta Crystallogr. Sect. C* **1997**, *53*, 167–169.
[51] M. S. Song, Y. M. Kang, Y. Il Kim, K. S. Park, H. S. Kwon, *Inorg. Chem.* **2009**, *48*, 8271–8275.
[52] V. I. Voronin, E. A. Sherstobitova, V. A. Blatov, G. S. Shekhtman, *J. Solid State Chem.* **2014**, *211*, 170–175.
[53] B. Raguž, K. Wittich, R. Glaum, *Eur. J. Inorg. Chem.* **2019**, *2019*, 1688–1696.
[54] Z. A. Grady, C. J. Wilkinson, C. A. Randall, J. C. Mauro, *Front. Energy Res.* **2020**, *8*, 1–23.
[55] A. Stock, B. Hoffmann, *Ber. Dtsch. Chem. Ges.* **1903**, *36*, 314–319.
[56] A. A. Coelho, *TOPAS Academic Version 6*, Coelho Software, Brisbane, Australia, **2016**.
[57] G. Oszlányi, A. Sütő, *Acta Crystallogr. Sect. A* **2004**, *60*, 134–141.
[58] G. Oszlányi, A. Sütő, *Acta Crystallogr. Sect. A* **2008**, *64*, 123–134.
[59] A. A. Coelho, *Acta Crystallogr. Sect. A* **2007**, *63*, 400–406.
[60] R. W. Cheary, A. A. Coelho, *J. Appl. Crystallogr.* **1992**, *25*, 109–121.
[61] R. W. Cheary, A. A. Coelho, J. P. Cline, *J. Res. Natl. Inst. Stand. Technol.* **2004**, *109*, 1–25.
[62] Bruker, *APEX3V2018.1-0*, **2018**.
[63] Bruker, *Topspin v.3.0 Pl 3*, Bruker Biospin GmbH, Germany, **2010**.
[64] Bruker, *OPUS 6.5*, Bruker Optik GmbH, Ettlingen, Germany, **2007**.

Manuscript received: September 23, 2022
Accepted manuscript online: November 16, 2022
Version of record online: December 27, 2022